Electronic Supplementary Material (ESI) for Energy & Environmental Science.
This journal is © The Royal Society of Chemistry 2015

Electronic Supporting Information

Mesoporous $Ni_{60}Fe_{30}Mn_{10}$-alloy based metal/metal oxide composite thick films as highly active and robust oxygen evolution catalysts

Eric Detsi,*[a] John B. Cook,[a] Benjamin K. Lesel,[a] Christopher L. Turner,[a] Yu-Lun Liang[a], Shauna Robbennolt[a] and Sarah H. Tolbert*[abc]

[a]Department of Chemistry & Biochemistry, UCLA, Los Angeles, CA 90095-1569, USA.

[b]Department of Materials Science & Engineering, UCLA, Los Angeles, CA 90095, USA.

[c]The California NanoSystems Institute, UCLA, Los Angeles, CA 90095.

Text S1: Processing of the ternary and binary parent alloys.

The NiFeMn ternary alloy was made by melting together pure Ni *(Sigma Aldrich)*, Fe *(J.T. Baker)* and Mn *(Strem Chemicals)* using an electric arc furnace with ultra-high purity argon atmosphere. The three elements used to make our parent alloys were in the powder form. Those powders were thoroughly mixed at the proper stoichiometry ($Ni_{15}Fe_{20}Mn_{65}$ at. %, which corresponds to $Ni_{15.8}Fe_{20.1}Mn_{64.1}$ wt. %), and consolidated by pressing them into pellets at 2.5 tons of force in a 13 mm die. The samples were then melted using an electric arc furnace, under one atmosphere of ultra-high purity argon. Those samples were fully melted into the liquid state, then allowed to cool. The alloy button acquired a spherical shape, which is an indication that the 3 metallic components fully melted and mixed.[1,2] Next, the samples were flipped and re-melted a minimum of four times to ensure thorough mixing to produce a homogeneous alloy pellet. The local temperature used to melt the parent alloy ($Ni_{15}Fe_{20}Mn_{65}$ at. %) was around 1500°C, which is higher than the melting point of all of the compoenent elements (melting point Ni: 1453°C, melting point Fe: 1204°C, melting point Mn: 1244°C).

Two binary parent alloys with composition $Ni_{30}Mn_{70}$ at. % and $Fe_{40}Mn_{60}$ at. % were melted in a similar way and used to make mesoporous samples for control experiments.

The above parent alloys were then cold-rolled from an initial thickness of ~7 mm down to submillimeter thicknesses (~0.3 mm).[1,2] Since cold-rolling reduces the grain size in the material and introduces stresses and defects in the crystal structure,[2] our cold-rolling process was performed in 3 steps. We first took the pellet from ~ 7 mm down to ~2 mm, then from ~2 mm down to ~0.7 mm, and finally from ~0.7 mm down to ~0.3 mm. Between each of these cold-rolling steps, the material was heated at 750°C for 30 minutes under flowing argon. These heat treatment steps were performed to recrystallize the material and release stresses introduced during the cold-rolling steps.[2]

Text S2: Faradaic efficiency

The water displacement method was used to determine the amount of gas oxygen gas produced during oxygen evolution.[3,4] Our setup is illustrated in Figure S1 below. It consists of 3 compartments: (1) The reaction chamber were gases are produced; (2) the gas transfer compartment; (3) the water displacement unit, consisting of a graduated cylinder divided into 10 µl increments. The following steps were performed for an accurate measurement of the volume of water displaced in the graduated cylinder: First, the solutions in the reaction chamber and in the gas transfer compartment were saturated with oxygen and hydrogen gases. Next, our mesoporous catalyst was used to oxidize water and produce gases, until the water level in the graduated cylinder starts to raise. This preliminary step was aimed at making sure that the tube connecting the different compartments are filled with produced gases. Finally, an electric charge (3.1 C) was passed through the catalyst until the water level in the graduated cylinder increases with 500 µl, corresponding to a pressure change of about $4.8x10^{-3}$ atm. We associate the 500 µl water displacement with hydrogen (2/3 of the total volume displaced) and oxygen (1/3 of the total volume displaced) gases produced during water oxidation from our mesoporous catalyst. The corresponding measured volume of oxygen is ~167 µl. We note, however, that while the abovementioned pressure change is not terribly high, it should result in an increased O_2 solubility in water of 31 µl O_2/l H_2O. Given that our whole apparatus contains 760 ml of water, this should correspond to an additional 24 µl of dissolved O_2. The total volume of oxygen produced is then is then ~191 µl, which requires 3.01 C of charge to generate, based on the 4-electron reaction: $4OH^- \rightarrow O_2 + 2\ H_2O + 4e^-$. The faradaic efficiency for oxygen evolution is then calculated as the ratio of the anodic output charge (3.01 C) to the anodic input charge (3.10 C) and was found to be 97%.

Figure S1: Water displacement setup

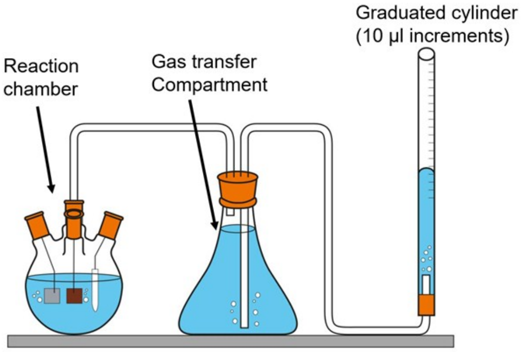

Figure S1. Illustration of the water displacement setup used the measure the volume of oxygen and hydrogen produced during water electrooxidation.

Text S3: Free-corrosion dealloying & dimensions of dealloyed samples used for water oxidation

Synthesis of mesoporous $Ni_{60}Fe_{30}Mn_{10}$ metal/metal oxide composites

The selective removal of Mn and Fe from the $Ni_{15}Fe_{20}Mn_{65}$ at % parent alloy was performed in a 1 M aqueous solution of $(NH4)_2SO_4$ *(Sigma Aldrich)*. The total corrosion time depends on the thickness of the parent alloy and on the amount of residual Mn that can be tolerated in the final dealloyed material. In the case of a 300 µm-thick parent alloy, 48 hours were required to take the content of Mn and Fe from $Ni_{15}Fe_{20}Mn_{65}$ at.% down to $Ni_{60}Fe_{30}Mn_{10}$ at.%. Note that during the free-corrosion process, the 1 M $(NH4)_2SO_4$ corroding solution turns brown. We attribute the brown color to ferric ions (Fe^{3+}). Fe from the parent alloy likely dissolves in the form of ferrous ions (Fe^{2+}), which are then further oxidized to ferric ions in solution. During the free-corrosion process, the brown solution was periodically (~every 4 hours) replaced by a fresh 1 M $(NH4)_2SO_4$ corroding solution.

The dealloyed material was rinsed in DI water and then in ethanol followed by drying in an argon atmosphere. Note that direct exposure of the sample to air for drying can cause it to ignite if it is not fully dealloyed. Ignition is attributed to the burning of residual Mn metal in air.

Synthesis of mesoporous $Ni_{90}Mn_{10}$ metal/metal oxide and mesoporous $Fe_{90}Mn_{10}$ metal/metal oxide

To make these materials, binary alloys with compositions $Ni_{30}Mn_{70}$ at. % and $Fe_{40}Mn_{60}$ at. % were first made, as mentioned in Text S1 above, and used as parent alloys for the synthesis of porous $Ni_{90}Mn_{10}$ and porous $Fe_{90}Mn_{10}$ by selective removal of Mn. Mn was then selective removed in a 1 M aqueous solution of $(NH4)_2SO_4$, again following the procedure described above. In the case of the $Ni_{30}Mn_{70}$ system, the 1 M aqueous $(NH4)_2SO_4$ corroding solution of does not turn brown because there is no Fe in this material system. The minimum dealloying time needed to bring the Mn content down to 10 at. % was also 48 hours for ~300 µm-thick samples of both $Ni_{30}Mn_{70}$ and $Fe_{40}Mn_{60}$. At the end of dealloying, a monolithic piece of mesoporous $Ni_{90}Mn_{10}$ is obtained. In the case of the $Fe_{40}Mn_{60}$ system, the initial amount of Fe was intentionally kept high (40 at %) to compensate for Fe dissolution during the free-corrosion process. Despite this fact, in contrast to the monolithic piece of mesoporous $Ni_{90}Mn_{10}$, dealloyed mesoporous $Fe_{40}Mn_{60}$ exhibits very poor mechanical stability and tends to break up into smaller pieces.

Dimensions of dealloyed samples used for water oxidation

Due to the robustness of our catalyst, the size of film was adjusted as shown below, depending on the experiment. These adjustments were needed in order to avoid currents beyond the limits of our potentiostat during water oxidation:

- Experiments in 0.1 - 0.3 M KOH: Film dimensions (Length x width x thickness) = (10 mm x 10 mm x 0.3 mm). Corresponding weight: ~ 76 mg.
- Experiments in 0.5 M KOH: Film dimensions (Length x width x thickness) = (10 mm x 0.5 mm x 0.3 mm). Corresponding weight: ~ 38 mg.
- Experiments in 1 M KOH: Film dimensions (Length x width x thickness) = (0.5 mm x 0.5 mm x 0.3 mm). Corresponding weight: ~ 19 mg.

Figure S2: Local surface composition studied by XPS ***(See also Text S4 for the effect of the local surface composition on the performance of our mesoporous catalyst).*** Since both EDS and WDS give the "bulk" composition of the mesoporous catalyst, X-ray Photoelectron Spectroscopy (XPS) was used to analyze the "surface" composition as well. Figure S2 below shows the typical XPS spectra for the elements present at the surface of our mesoporous catalyst. XPS provides information on both metal oxidation state and on local surface composition. The data presented below produces a local surface composition of 76 at. % Ni, 16 at. % Fe, and 8 at. % Mn for a mesoporous catalyst with bulk composition 60 at. % Ni, 30 at. % Fe, and 10 at. % Mn. The data thus indicates that there is a small depletion of the more oxidatively unstable elements (Mn and Fe) at the catalyst surface.

Oxidation state data from XPS is also consistent with the TEM image shown in figure 2 of the manuscript, which shows a metal core completely surrounded by a metal oxide shell. All data can be fit with a single oxidation state for each element, corresponding to various metal oxides or metal hydroxides. The Ni 3p region shows a spin orbit split pair of peaks corresponding to $3p_{1/2}$ and $3p_{3/2}$. Because of the small splitting, much of the literature fits this 3p data to a single peak, and based on the single peak position, the sample surface is likely composed mostly of Ni^{3+} like that found in NiOOH, though a mixture of $Ni(OH)_2$ and NiOOH is also consistent with the data.[5] There is also a satellite peak, in good agreement with previous reports.[5] Spin orbit splittings for the 3p peak of Fe and Mn are too small to resolve, so both of these regions were fit with a single peak. The Mn peak indicates an oxidation state of 2^+, consistent with either a mixed metal oxide like $MnFe_2O_4$ or MnO.[6] Finally, the Fe peak position corresponds to Fe^{3+}, as found in mixed metal oxides like $NiFe_2O_4$ or iron oxyhydroxides like FeOOH.[6,7]

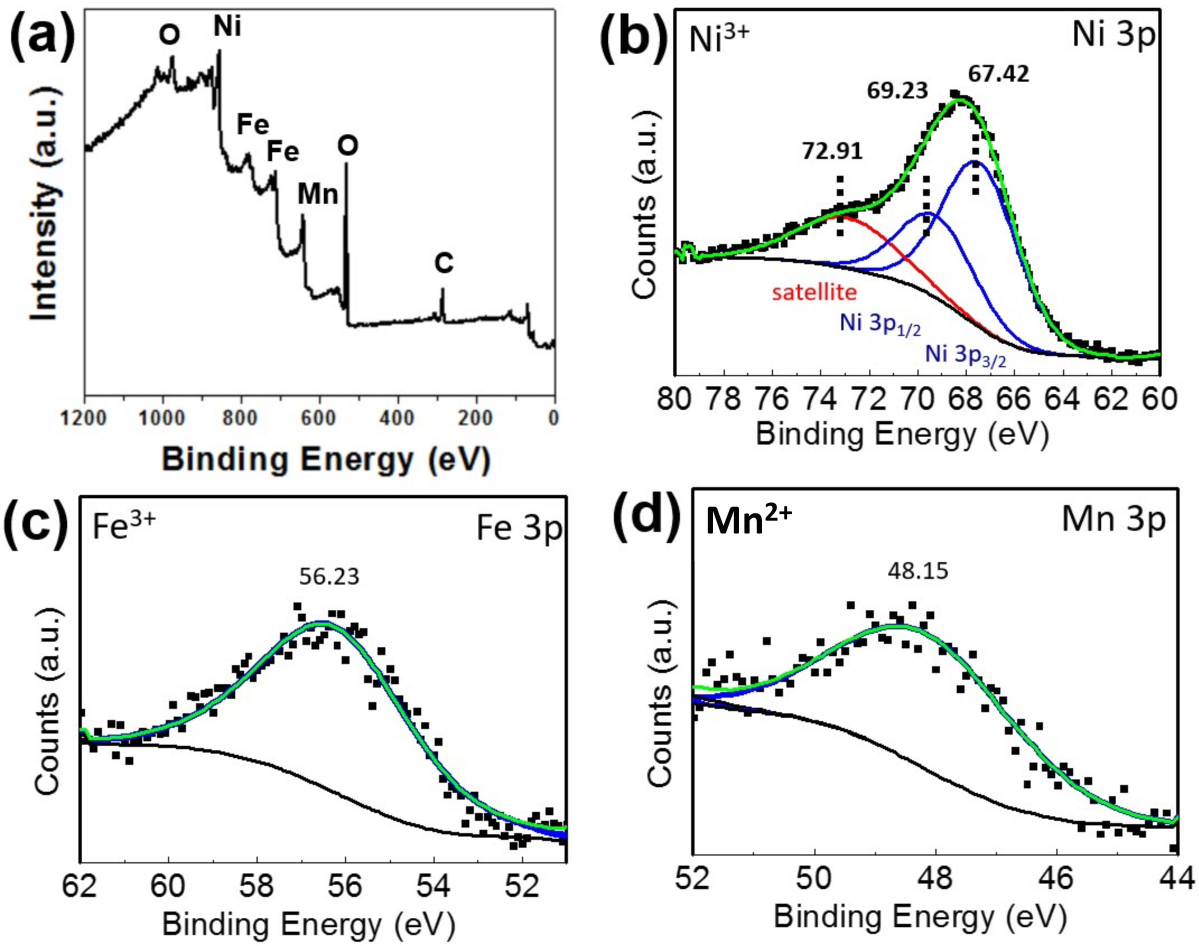

Figure S2. (a) XPS survey spectrum of the surface of the of our mesoporous NiFeMn-based catalyst. Panels (b) – (d) show high resolution scans in the metal 3p regions. Data is shown for Ni 3p (b), Fe 3p (c), and Mn 3p (d). All data can be well fit with a single oxidation state corresponding to Ni^{3+}, Fe^{3+}, and Mn^{2+}.

Figure S3: X-ray diffraction (XRD) of mesoporous $Ni_{90}Mn_{10}$ at. %

XRD of dealloyed mesoporous $Ni_{90}Mn_{10}$ at. %. The materials is crystalline, with a crystal structure very similar to pure Ni. Some broad diffraction peaks from manganese oxide are also observed. The crystal structure is quite different from dealloyed mesoporous $Ni_{60}Fe_{30}Mn_{10}$, as presented in Fig. 1c in the main manuscript, which shows no crystalline diffraction peaks.

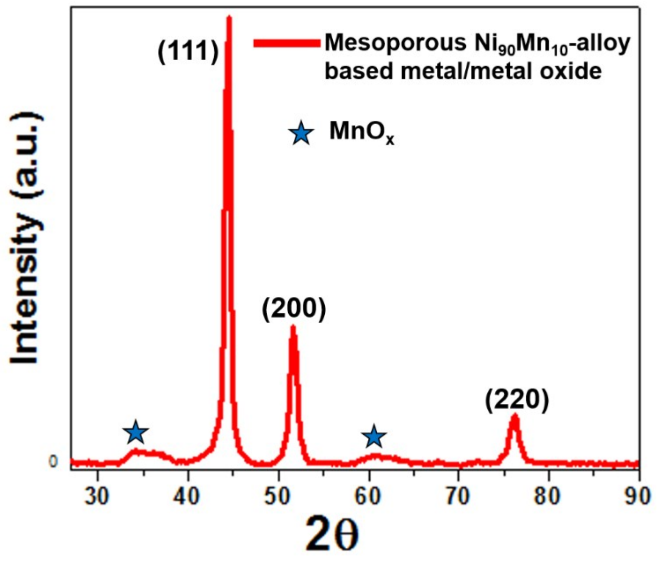

Text S4: Role of Mn on the performance of our mesoporoys NiFeMn-based catalyst.

The effect of transition metal doping including Mn- and Fe-doping, on the catalytic activity of Ni-based double hydroxides towards oxygen evolution was recently investigated in a combined theoretical & experimental work on Ni-based double hydroxide electrocatalysts for the oxygen evolution reaction, by Diaz-Morales *et al.*[8] They suggested that in Ni-based double hydroxides catalysts, the active sites are oxyhydroxide type in the form NiMOOH, where M is a transition-metal dopant (Fe, Mn…), in which the metals form octahedral NiO_6 and MO_6 complexes. Applying that to our mesoporous NiFeMn-based catalyst, we can conclude that the primary active sites should be Fe-doped Ni oxides (NiFeOOH). In addition, since XPS data reveals the presence of some Mn at the surface of our mesoporous NiFeMn-based catalyst, we can hypothesize that Mn-doped Ni oxides (NiMnOOH) could represent another active sites. In that same work, the authors also performed one-by-one comparisons between $Ni(OH)_2$ and the double hydroxides, and between the double hydroxides and a state-of-the-art IrO_2 catalyst. They observed the following activity trends:

- NiFe-Oxide > NiMn-Oxide > $Ni(OH)_2$
- NiFe-Oxide > NiMn-Oxide> IrO_2

In the case of NiFe-oxides, it is already well-recognized that Fe-doping improves the performance of Ni oxides for oxygen evolution reaction. In the case of NiMn-oxide, their work clearly shows that Mn-doping also improves the performance of Ni oxides for evolution reaction. In particular, NiMn-Oxide performs better than both undoped nickel oxide [$Ni(OH)_2$] and the state-of-the art IrO_2 catalyst. This suggests that the residual Mn-doping in our mesoporous NiFeMn-based catalyst may play an active role in the oxygen evolution reaction. We note, however, that since the activity of NiFe-Oxide > NiMn-Oxide,[8] we believe that the overall performance of our mesoporous NiFeMn-based catalyst could improve further if there was no residual Mn in our mesoporous material system. Note also that the presence of residual Mn might explain why the Tafel slope of our mesoporous NiFeMn-based catalyst is somewhat higher than those reported in literature for optimized NiFe-based catalysts.

While this higher Tafel slope is not ideal, it may be that the residual Mn improves the overall corrosion resistance behavior of our mesoporous NiFeMn-based catalyst in alkaline solution,[9] as discussed in section 3.4.4 of the manuscript.

Figure S4: Nitrogen porosimetry data for the mesoporous NiFeMn-based catalyst.

The BET surface area is ~43 m^2/g. The average pore size determined from the volume weight BJH pore size distribution is ~10 nm (Figure S4b). This value is in good agreement with the pore size determined from SEM images.

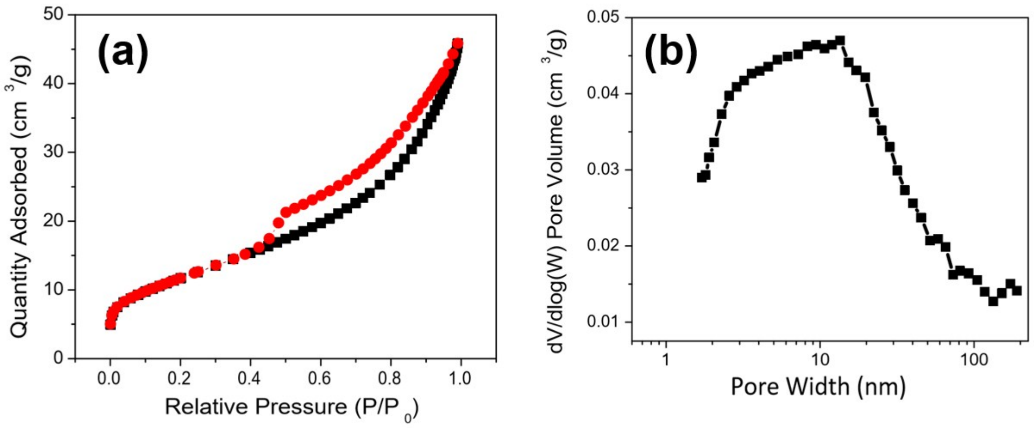

Figure S4. Nitrogen porosimetry data for the mesoporous NiFeMn-based catalyst. Part (a) shows the raw adsorption (black) and desorption (red) isotherms. Part (b) show the volume weighted BJH pore size distribution determined from the adsorption branch of the isotherm. The BET surface area is ~43 m^2/g. The average pore size is ~10 nm.

Figure S5: Nitrogen porosimetry data for the mesoporous $Ni_{90}Mn_{10}$-based control sample.

The BET surface area is ~103 m^2/g. The pore size distribution determined from the nitrogen adsorption is in the range between ~3-9 nm (Figure S5-b).

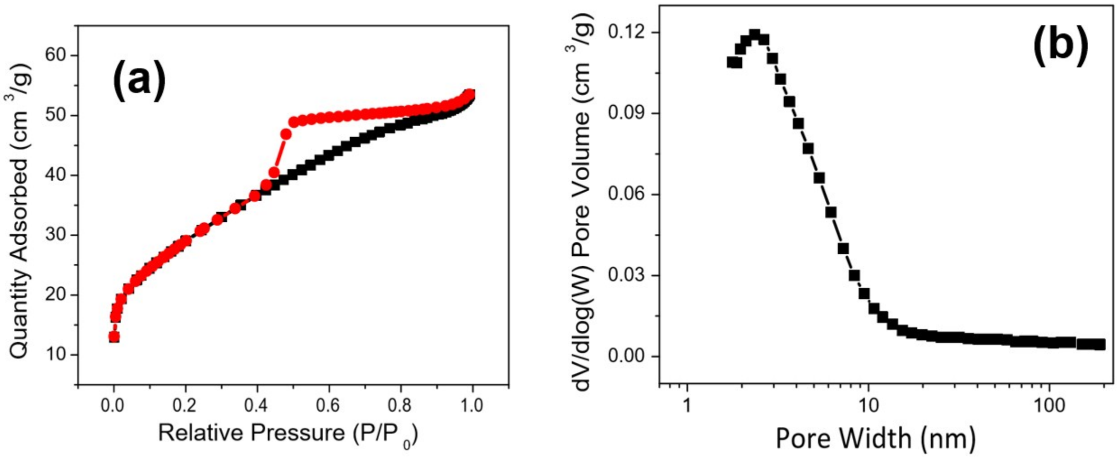

Figure S5. Nitrogen porosimetry data for the mesoporous $Ni_{90}Mn_{10}$-based catalyst. Part (a) shows the raw adsorption (black) and desorption (red) isotherms. Part (b) show the volume weighted BJH pore size distribution determined from the adsorption branch of the isotherm. The BET surface area is 103 m^2/g. The majority of pores are found in the range between 3 and 9 nm.

Figure S6: Nitrogen porosimetry data for the mesoporous $Fe_{90}Mn_{10}$-based control sample.

The BET surface area is ~206 m^2/g. The majority of pores are found in the range between 2 and 30 nm.

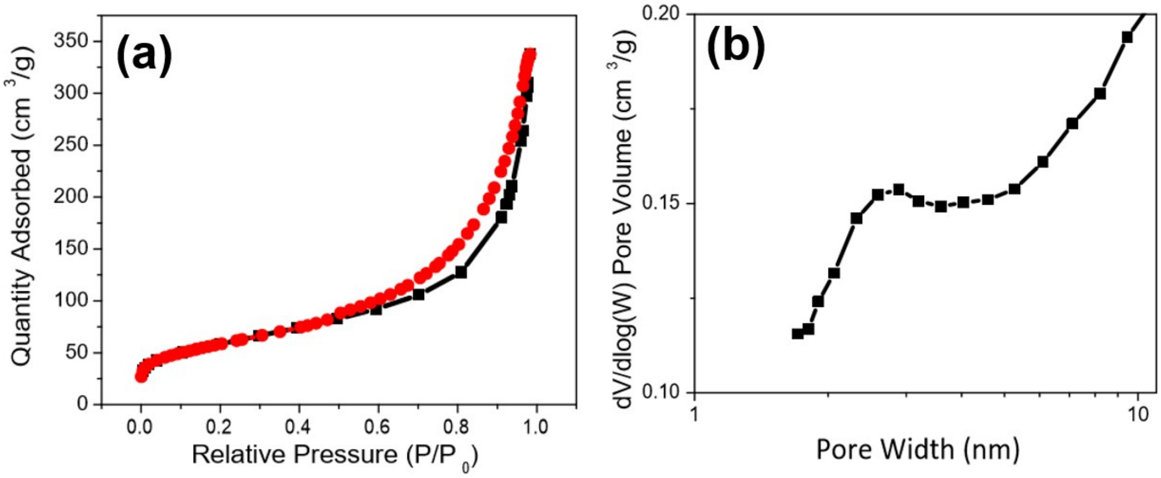

Figure S6. Nitrogen porosimetry data for the mesoporous $Fe_{90}Mn_{10}$-based control sample. Part (a) shows the raw adsorption (black) and desorption (red) isotherms. Part (b) show the volume weighted BJH pore size distribution determined from the adsorption branch of the isotherm. The BET surface area is 206 m^2/g. The majority of pores are found in the range between 2 and 30 nm.

Text S5: Determination of the solid bulk density of $N_{i60}Fe_{30}Mn_{10}$

According to references,[10,11] "ρ" in Equation 1: *(S=C/ρd$_L$)* should be the "solid bulk" density of a NiFeMn ternary alloy with bulk (dense) composition. $Ni_{60}Fe_{30}Mn_{10}$. Thus the density ρ was determined as follows:

$$\rho = (0.6*\text{density Ni}) + (0.30*\text{density Fe}) + (0.10*\text{density Mn})$$

$$\rho = (0.6*\ 8.91\ g/cm^3) + (0.30*7.87\ g/cm^3) + (0.10*7.21\ g/cm^3)$$

$$\rho \approx 8.43\ g/cm^3$$

Figure S7: Cyclic voltammograms of a free standing mesoporous NiFeMn-based catalyst in 1 M KOH (red) and 0.1 M KOH (black).

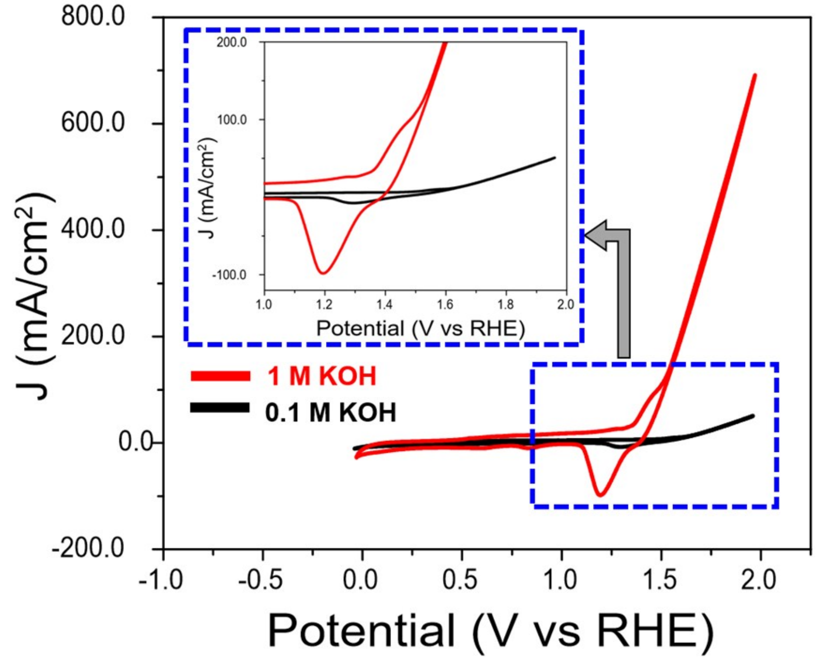

Figure S7. Cyclic voltammograms of a free standing mesoporous NiFeMn-based catalyst in 1M KOH (red) and 0.1 M KOH (black).

Figure S8: Linear sweep voltammograms of our free standing mesoporous NiFeMn-based catalyst in 1 M KOH (red) and 0.1 M KOH (black).

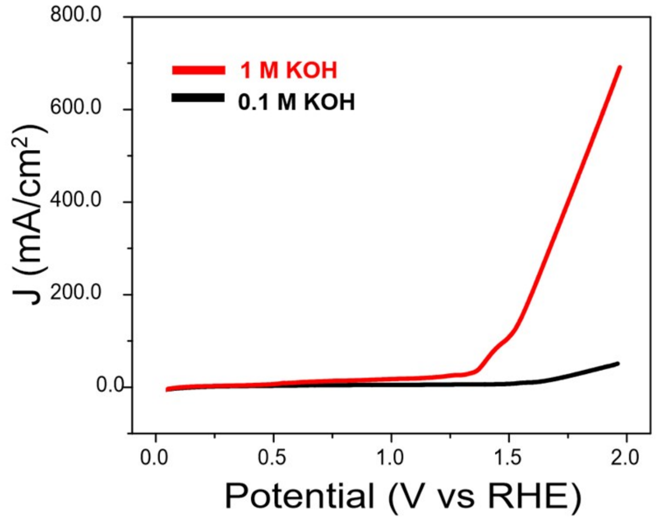

Figure S8. Linear sweep voltammograms of a free standing mesoporous NiFeMn-based catalyst in 1M KOH (red) and 0.1 M KOH (black).

Table S1: Overview of the BET surface areas and pore size distributions for our optimized sample and for two control samples.

	Main sample	**Control sample 1**	**Control sample 2**
Bulk composition	Mesoporous $Ni_{60}Fe_{30}Mn_{10}$	Mesoporous $Ni_{90}Mn_{10}$	Mesoporous $Fe_{90}Mn_{10}$
BET surface area (see Fig. S4, S5& S6 above)	43 m^2/g	~103 m^2/g	~206 m^2/g
pore size distribution (from BET porosimetry)	~2-70 nm (with average ~10 nm)	~3-9 nm	~2-30 nm

Figure S9: Electrocatalytic performance as a function of elemental composition for a series of catalysts with different bulk compositions. Despite the fact that a range of compositions were examined, the electrochemistry data is remarkably similar. From this data, we conclude that this catalyst system is actually quite forgiving to the details of elemental composition, and a broad range of compositions around the optimal value give almost identical results.

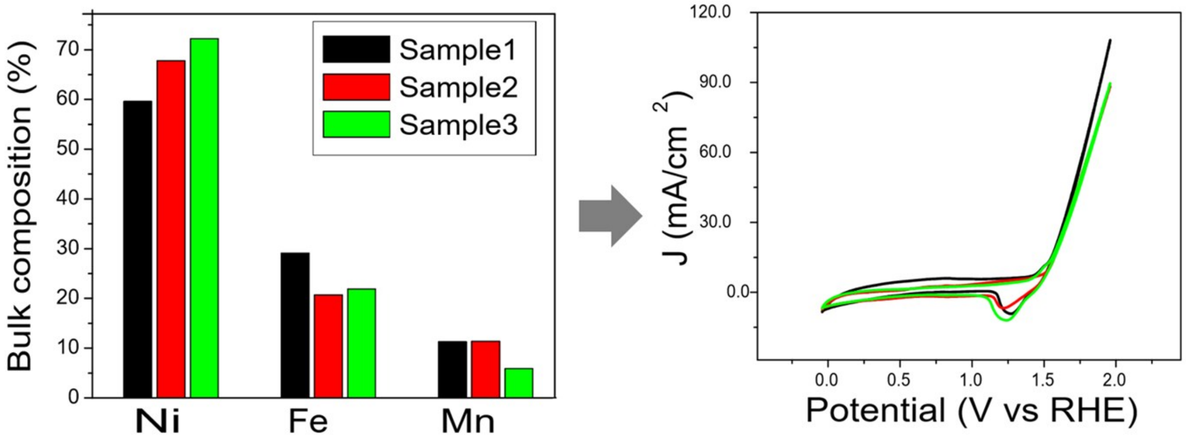

Figure S9. Effect of bulk composition on the performance of the mesoporous NiFeMn-based catalyst. The left graph shows the composition of three different samples, made from three different alloys with different elemental ratios. Elemental composition was determined using EDS. The right graph shows CVs taken in 0.3 M KOH at the sweep rate of 1 mV/s. Despite the differences in elemental composition, the electrochemical performance of the three samples is remarkably similar, suggesting the system is fairly insensitive to the details of atomic composition.

Figure S10: Illustration of the Ni foam foil/mesoporous NiFeMn sandwhich configuration used for long term stability testing. The purpose of the Ni foam foal is to add mechancal stability to the mesoporous catalyst so that the electrolty can be stirred during the electrocatalytic reaction.

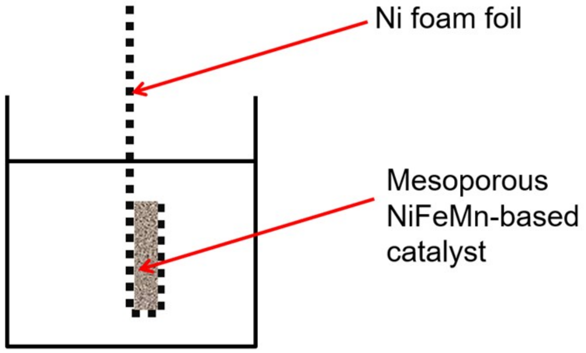

Figure S10. Schematic of the electrode structure used for long term stability testing of our mesoporous NiFeMn based catalyst.

Figure S11: Stability tests performed on the "empty" nickel foam. In Figure S11-a below, it can be seen that the nickel foam exhibits a very poor stability, as mentioned in the manuscript: At a current density of 500 mA/cm^2, water oxidation on the nickel foam starts at 1.79 V versus RHE (560 mV overpotential). Within an hour, the water oxidation potential further increases from 1.79 V versus RHE to the set upper voltage limit of 2 V versus RHE, corresponding to an overpotential of 770 mV (dashed red line). In contrast, when the nickel foam is loaded with our mesoporous catalyst, water oxidation takes place over 11 days at 1.59 V versus RHE, corresponding to 360 mV overpotential (dashed green line). Even at a relatively lower current density of 100 mA/cm^2 the "empty" nickel foam fails to oxidize water after 3 hours (Figure S11-b). The oscillatory behavior that follows is indicative of the failure of the nickel foam to oxidize water at the applied current density. Because the set current density cannot be achieved, the voltage drops to the lower set limit, followed by another attempt to oxidize water at higher overpotentials. Hence the oscillatory behavior.

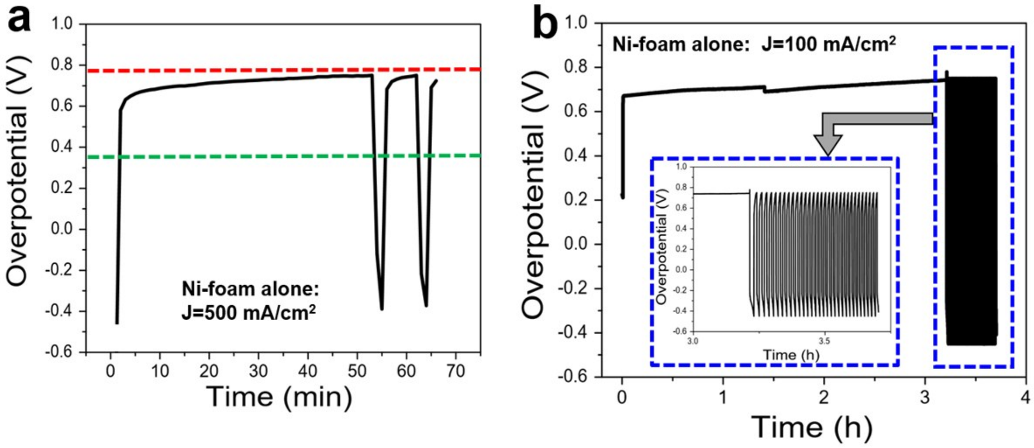

Figure S11. (a) Stability test on an "empty" Ni-foam at 500 mA/cm^2. The nickel foam catalyst lasts for about 1 hour. The dashed line represents the overpotential recorded when the nickel foam is loaded with our mesoporous NiFeMn-based catalyst. The NiFeMn catalyst is stable for over 11 days. The red dashed line represents the maximum overpotential allowed during our experiments. **(b)** Stability tests on "empty" Ni-foams at 100 mA/cm^2. Even at lower current density, the nickel foam catalyst only last for about 3 hours.

References:

1 E. Detsi, Z. Vuković, S. Punzhin, P. M. Bronsveld, P. R. Onck and J. T. M. De Hosson, *CrystEngComm*, 2012, **14**, 5402.

2 E. Detsi, S. Punzhin, J. Rao, P. R. Onck and J. T. M. De Hosson, *ACS Nano*, 2012, **6**, 3734–3744.

3 A. Paracchino, V. Laporte, K. Sivula, M. Grätzel and E. Thimsen, *Nat. Mater.*, 2011, **10**, 456–461.

4 Z. Chen, C. Lv, Z. Chen, L. Jin, J. Wang and Z. Huang, 2014, 1200–1213.

5 K. K. Lian, D. W. Kirk and S. J. Thorpe, *J. Electrochem. Soc.*, 1995, **142**, 3704 – 3712.

6 G. C. Allen, S. J. Harris, J. A. Jutson and J. M. Dyke, *Appl. Surf. Sci.*, 1989, **37**, 111–134.

7 N. S. McIntyre and D. G. Zetaruk, *Anal. Chem.*, 1977, **49**, 1521–1529.

8 O. Diaz-Morales, F. Calle-Vallejo, C. de Munck and M. T. M. Koper, *Chem. Sci.*, 2013, **4**, 2334.

9 R. Subbaraman, D. Tripkovic, K. Chang, D. Strmcnik, A. P. Paulikas, P. Hirunsit, M. Chan, J. Greeley, V. Stamenkovic and N. M. Markovic, *Nat. Mater.*, 2012, **11**, 550–557.

10 E. Detsi, E. De Jong, a. Zinchenko, Z. Vuković, I. Vuković, S. Punzhin, K. Loos, G. Ten Brinke, H. a. De Raedt, P. R. Onck and J. T. M. De Hosson, *Acta Mater.*, 2011, **59**, 7488–7497.

11 Y. H. Tan, J. a. Davis, K. Fujikawa, N. V. Ganesh, A. V. Demchenko and K. J. Stine, *J. Mater. Chem.*, 2012, **22**, 6733.